Using Landsat Surface Reflectance Data as a Reference Target for Multiswath Hyperspectral Data Collected Over Mixed Agricultural Rangeland Areas

Cooper McCann, Kevin S. Repasky, Mikindra Morin, Rick L. Lawrence, and Scott Powell

***Abstract*— Low-cost flight-based hyperspectral imaging systems have the potential to provide important information for ecosystem and environmental studies as well as aide in land management. To realize this potential, methods must be developed to provide large-area surface reflectance data allowing for temporal data sets at the mesoscale. This paper describes a bootstrap method of producing a large-area, radiometrically referenced hyperspectral data set using the Landsat surface reflectance (LaSRC) data product as a reference target. The bootstrap method uses standard hyperspectral processing techniques that are extended to remove uneven illumination conditions between flight passes, allowing for radiometrically self-consistent data after mosaicking. Through selective spectral and spatial resampling, LaSRC data are used as a radiometric reference target. Advantages of the bootstrap method include the need for minimal site access, no ancillary instrumentation, and automated data processing. Data from two hyperspectral flights over the same managed agricultural and unmanaged range land covering approximately 5.8 km^2 acquired on June 21, 2014 and June 24, 2015 are presented. Data from a flight over agricultural land collected on June 6, 2016 are compared with concurrently collected ground-based reflectance spectra as a means of validation.**

***Index Terms*— Agriculture, algorithms, remote sensing, vegetation, vegetation mapping.**

I. Introduction

IMAGING spectrometers record the reflectance spectra for each pixel in a digital image, and contained within the reflectance spectra is a wealth of information that can be exploited for a variety of environmental and ecosystem studies. For example, vegetation has many spectral features in the visible, near-infrared (NIR), and shortwave-infrared wavelengths. These include photosynthetic pigments that absorb in the 400–700 nm range, the red edge in the 700–750 nm range, resulting from chlorophyll [1]–[3], liquid water inflection at 1080–1170 nm [4], the absorption of various leaf waxes and oils in the 1700–1780 nm range, and cellulose absorption around 2100 nm, while spectral features associated with soil properties appear between 2100–2300 nm [5], [6]. Using these spectral features, a variety of applications have emerged including precision agriculture [7]–[11], noxious weed mapping for rangeland management [12], [13], forest health monitoring [14], [15], and vegetation stress analysis [16], [17] for carbon sequestration site monitoring [18]–[24]. In addition, nonvegetation-based uses such as mineral identification/detection [25], [26] and potential military applications [27] are possible. Many extensions of these applications to management implementations require a temporal series of data over broad spatial scales, which lead to the need to mosaic data from multiple flight paths and to radiometrically calibrate these mosaicked data to a trusted reference. This directly leads to the research problem addressed in this paper: how to obtain large-area, radiometrically referenced hyperspectral data using a low-cost system with minimal ancillary instrumentation, limited access to the study site, and the capability for automated data processing.

Imaging spectrometers for large-area studies can be deployed on a variety of platforms including satellites, aircraft, and unmanned aerial vehicles [28]. One of the most prominent satellite-based spectrometers is the operational land imager (OLI) onboard the Landsat 8 satellite, which images the earth every 16 days and provides 30-m spatial resolution in ten distinct bands and 15-m spatial resolution in the panchromatic band [29], [30]. The Hyperion sensor onboard the EO-1 satellite provides spectral imaging with 220 bands between 400 and 2500 nm with a 30-m spatial resolution [31], [32], making it a truly hyperspectral sensor. While the Hyperion provides 220 bands compared to the ten bands for the OLI, it does not provide full global coverage.

While spectral imaging instruments aboard satellites can provide global coverage and thereby a synoptic view of the earth's ecosystems, flight-based imaging spectrometers can provide a cost-effective remote sensing tool for mesoscale studies with spatial resolution on the order of 1 m. State-of-the-art systems such as Airborne Visible/Infrared Imaging Spectrometer (AVIRIS) bridge the gap between satellite imagers and smaller, less expensive flight-based imaging

Manuscript received May 11, 2016; revised September 9, 2016, October 25, 2016, and February 2, 2017; accepted April 11, 2017. Date of publication July 25, 2017; date of current version August 25, 2017. This work was supported in part by the U.S. Department of Energy and the National Energy Technology Laboratory under Award DE-FC26-05NT42587 and in part by an agency of the U.S. Government. *(Corresponding author: Kevin S. Repasky.)*

This paper has supplementary downloadable material available at http://ieeexplore.ieee.org, provided by the authors. This includes Matlab programs. This material is 78 kB in size.

C. McCann is with Montana State University, Bozeman, MT 59717 USA (e-mail: cooper.mccann@montana.edu).

K. S. Repasky is with the Electrical and Computer Engineering Department, Montana State University, Bozeman, MT 59717 USA (e-mail: repasky@ece.montana.edu).

M. Morin, R. L. Lawrence, and S. Powell are with the Land Resources and Environmental Sciences Department, Montana State University, Bozeman, MT 59717 USA (e-mail: mikindra.morin@gmail.com; rickl@montana.edu; spowell@montana.edu).

Color versions of one or more of the figures in this paper are available online at http://ieeexplore.ieee.org.

Digital Object Identifier 10.1109/TGRS.2017.2699618

spectrometers such as those used in this paper. The AVIRIS system covers a wavelength range of 400–2500 nm in 224 bands and, depending upon the flight altitude, returns orthorectified and radiometrically calibrated data with a spatial resolution of either 20 or 4 m [33] after postflight processing. While the system used in this paper is not as technically advanced as AVIRIS, it can provide hyperspectral data at a much lower cost and can provide a temporal series of hyperspectral data for a variety of applications such as ecosystem studies and precision agriculture.

Radiometric correction of the output of hyperspectral imagers rely upon the same types of calibration processes used for satellites [34], [35]. Simpler systems are limited to preflight calibrations performed in a laboratory setting while more advanced large-scale systems such as HyMap [36] and AVIRIS possess on-board calibrations and vicarious calibrations applied to the data during postprocessing. Even with the quality of some well-characterized data products, absolute surface reflectance products are limited to a relatively small number of studies that have used ground-based sensors and advanced atmospheric modeling to calibrate the flight data [37], [38]. Additionally, most studies have been limited to single swaths [39], and while some studies have used multiple flight passes to create broader areas of study, the artifacts present after mosaicking can often obscure the desired results [40]. Furthermore, there have been limited studies that leverage the different strengths of satellite data and hyperspectral data together [41].

This paper presents a method for: 1) combining hyperspectral data from multiple flight paths while minimizing the effects of uneven illumination and 2) radiometrically correcting the mosaicked data to the readily available provisional Landsat surface reflectance (LaSRC) product data to produce large-area radiometrically referenced surface reflectance data. The radiometric data from Landsat 8 was used as the reference standard owing to its quality of data in terms of calibration, signal-to-noise, global coverage, and quality of processing including atmospheric modeling [29], [30], [42]–[44]. The processing technique described in this paper has the potential to allow routine large-area hyperspectral data sets to be used for a variety of applications. This is in contrast to previous studies where calibration required ground-based instruments and advanced atmospheric modeling and provided limited spatial and temporal coverage [37]–[40].

To quantitatively verify the extent of correction achieved by this technique, the final hyperspectral data were tested against data taken at a test site. Also, hyperspectral data were compared to LaSRC data over thousands of random areas with varying sizes. Additionally, two subsequent years of data were compared as a means of demonstrating the variability present in the data that can be lost without radiometric calibration.

This paper is organized as follows. A description of the field site, hyperspectral imager, and data collection are presented in Section II. The processing steps used to create the geocorrected, mosaicked, and radiometrically referenced surface reflectance data are presented in Section III. The results are presented in Section IV. Discussion of the results and future improvements are discussed in Section V. Finally, some concluding comments are presented in Section VI. The MATLAB code used for processing is included in the Supplementary Online Material.

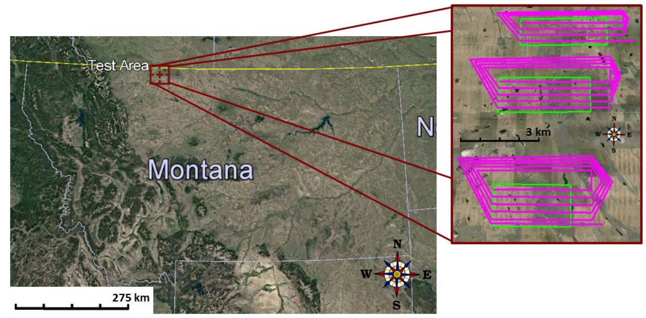

Fig. 1. Location of the BSCSP demonstration site in north-central Montana. Inset: Map of the three test areas (green) and flight paths (magenta) at the demonstration site. Site A is southernmost, site B is the center, and site C is the northernmost regions.

II. Experimental Methods

The primary study area (N48° 51′ 42″, W111° 44′ 13″, elevation 1143 m) is located in north-central Montana at the Big Sky Carbon Sequestration Partnership (BSCSP) demonstration site, as shown in Fig. 1. As part of this demonstration project, aerial monitoring of vegetation stress using hyperspectral data will be evaluated as a potential technique for monitoring the efficacy of below-ground CO_2 storage. The use of flight-based spectral imaging will require the direct comparison of data from multiple flights obtained during a single summer and also from year-to-year, therefore requiring a method for radiometrically referencing the spectral data. The region of interest examined herein, the northernmost region outlined in green in the inset of Fig. 1, was approximately 4350×1330 m^2, and contained regions of fallow fields, planted wheat/barley fields, scrub land, arroyos, draws, and some buildings and roadways. This landscape provided a number of challenges from the processing point of view because of the myriad of factors contributing to uneven illumination of the landscape, including topography, bidirectional reflectance, and changing cloud cover.

The hyperspectral imaging system used for this data collection consisted of an imaging spectrometer, a global positioning system/inertial navigation system (GPS/INS), and a flight computer all mounted on a custom-built aluminum plate and flown in a single-engine Cessna Skyhawk. The imaging spectrometer (Pika II from Resonon Inc., Bozeman, MT, USA) weighed 1.1 kg, had a spectral range of 425–925 nm, and was binned to provide 80 spectral channels with 6.39-nm spectral resolution. The imaging spectrometer was calibrated in the factory at the time of its manufacture. The GPS/INS (Micro INS, MIS-100-000 from Rockwell Collins, Cedar Rapids, IA, USA) was Wide Area Augmentation System enabled to improve the tracking accuracy of the GPS navigation, and it provided 0.2° pitch and roll accuracy. Hyperspectral data and GPS/INS data were transferred to a P-CAQ PC-104 format flight computer (Resonon Inc., Bozeman, MT, USA). Flights, shown in magenta in the inset of Fig. 1, were made approximately 1220 m above ground level with a 22.5° field of view lens on June 21, 2014 and June 24, 2015 taking approximately 18 min from 11:21 to 11:39 A.M. mountain daylight time for the region of interest. Data were taken in a push broom configuration that captured all spectral information in a single instant of time across an entire line perpendicular to the flight direction. Each line captured 640 pixels over 485 m, providing a 0.75-m cross-track resolution. The number of passes was chosen so that, even with the presence of slight turbulence, there would be an overlap between adjacent swaths of 100–150 m. This allowed adjacent swaths to be referenced to each other and guaranteed complete coverage of the test area. For the test area examined in this paper, site C in the northernmost test area in Fig. 1, four separate flight passes were flown wherein all were acquired from east to west to reduce issues associated with different look angles which produced four swaths that needed to be combined/mosaicked to produce the final hyperspectral data. Swaths are numbered 1–4 starting in the south and extending to the north.

Since it was not possible to access the site under study to collect data on the surface reflectance, a similar agricultural site was used instead. A winter wheat field located outside of Bozeman, MT (N45° 33′ 41′, W111° 10’ 26″, elevation 1461 m) was flown on June 02, 2016 with the same imaging system described above, but at an altitude of 600 m yielding 0.5-m pixels. Data were processed using the technique described in this paper with LaSRC data from six days after, June 08, 2016. Additionally, data were collected with an ASD Field Spec Pro 350 on the wheat in the field on the same day as the flight. The ASD is a 16-b spectrometer that has a spectral range of 350–2500 nm. The sampling interval for the instrument is 1.4 nm at 350–1000 nm and 2 nm at 1000–2500 nm.

III. PROCESSING

Data from site C from the flight on June 24, 2015 are used as the example data for the processing, with the flight data on June 21, 2014, processed using the same steps, being used for the year-to-year comparison shown in the results section.

The processing steps needed to convert raw hyperspectral data to large-area, radiometrically referenced surface reflectance hyperspectral data are shown in Fig. 2. The standard processing steps [45]–[47] that are readily available in most commercial software packages are shown outlined in dashed black, while additional processing steps are outlined in solid blue. With the exception of the type of georeferencing used, each of the steps can be automated, which makes this process ideal for large-area monitoring of remote areas where it is either unfeasible or impractical to deploy ancillary instruments or targets.

The processing flow can be broken into two separate phases. The first phase of the processing, shown in the top flowchart of Fig. 2, deals with the aspects of spatial processing and the steps necessary to combine raw flight-based hyperspectral data swaths with a self-consistent large-area data product. This final data product will be georeferenced to master data wherein individual swaths can be radiometrically calibrated to match their neighboring swaths. However, this final spatially calibrated large-area data lack the absolute radiance or reflectance values that are necessary for comparing areas separated from each other in space and/or time.

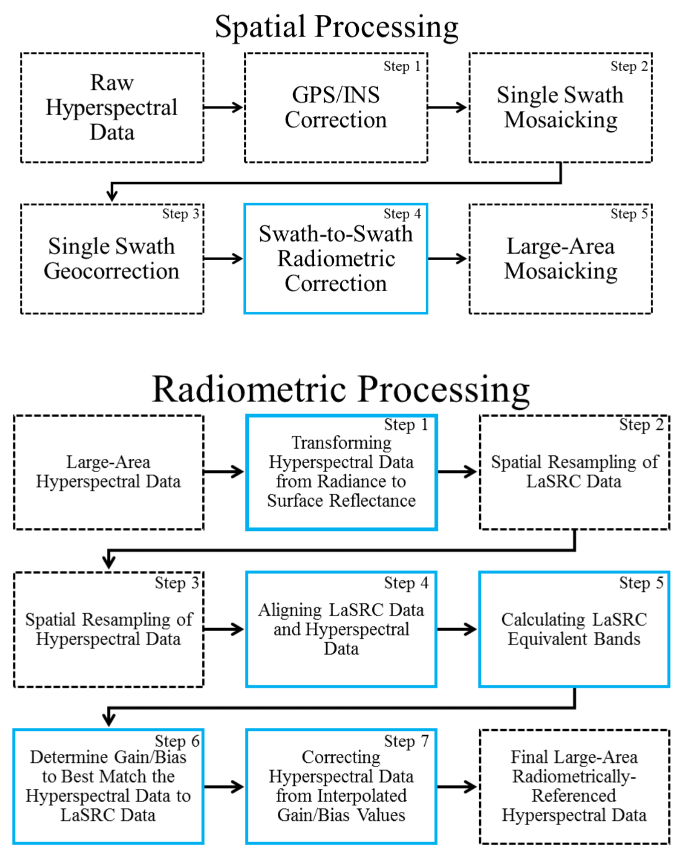

Fig. 2. Processing flowchart showing the steps to turn raw hyperspectral data into large-area radiometrically referenced surface reflectance hyperspectral data. Steps that extend beyond standard processing techniques (dashed black boxes) are outlined in solid blue. (Top) Spatial corrections required to assemble large-area hyperspectral data. (Bottom) Radiometric corrections needed to correct the hyperspectral data to surface reflectance values.

The second phase of the processing, shown in the bottom flowchart of Fig. 2, was applied to the spatially corrected radiometrically self-consistent data, resulting in radiometrically referenced surface reflectance data. This second phase constitutes removing solar irradiance from the hyperspectral data to obtain surface reflectance values and a subsequent selective spatial and spectral resampling of the data allowing for the hyperspectral surface reflectance data to be referenced to LaSRC data. Solar irradiance was removed based on a simple atmospheric model to obtain surface reflectance values for the hyperspectral data. Spatial processing involved resampling both the LaSRC data and the hyperspectral data to a common resolution so that the reflectance values could be compared on a pixel-by-pixel basis. Spectral processing involved resampling the hyperspectral data based on the Landsat spectral response curves to find what Landsat would measure given the hyperspectral data. After these two processing phases were completed, large-area, radiometrically referenced surface reflectance hyperspectral data were obtained.

A. Spatial Processing Steps 1 and 2: GPS/INS Correction and Single Swath Mosaicking

The raw hyperspectral data along with the GPS/INS information were processed using a postprocessing software (GeoReg Resonon, developed for Resonon Inc., by Space

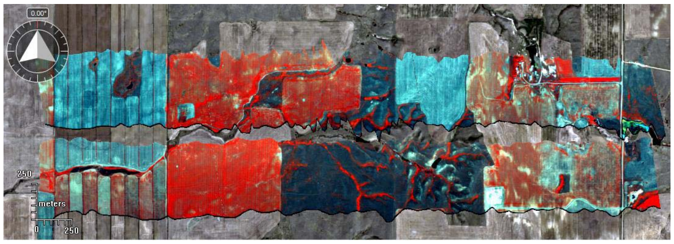

Fig. 3. Two separate swaths georeferenced to a USGS 0.3-m resolution orthoimage using at least 30 points per swath. Excellent spatial agreement can be achieved with this type of referencing and can be done without ever having to physically access the test area, making it ideal for remote regions or harsh terrain. Orthoimage is displayed in true color RGB with a standard deviation stretch. Swaths 2 and 4 are displayed independently with a standard deviation stretch in false-color IR using bands 10, 20, and 70 of the hyperspectral camera which correspond to 490.8, 554.7, and 874.2 nm.

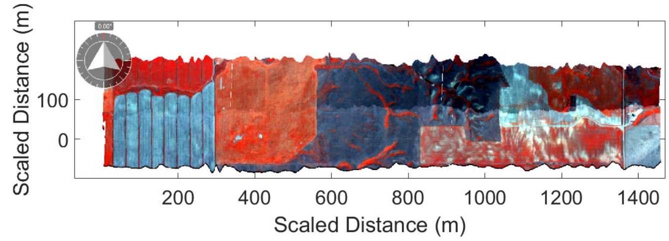

Fig. 4. Two adjacent geocorrected swaths (1 and 2) mosaicked together with no radiometric calibration. The swaths show the differing global illumination conditions between them, and also the changing lighting conditions along the northern swath that are most likely owing to high-altitude clouds. This illumination difference makes it impossible to have a self-consistent data when mosaicking multiple swaths with different illumination conditions. Scaled distances correlate with this figure as well as Figs. 5 and 6. The mosaic is displayed with a standard deviation stretch in false-color IR using bands 10, 20, and 70 of the hyperspectral camera which correspond to 490.8, 554.7, and 874.2 nm.

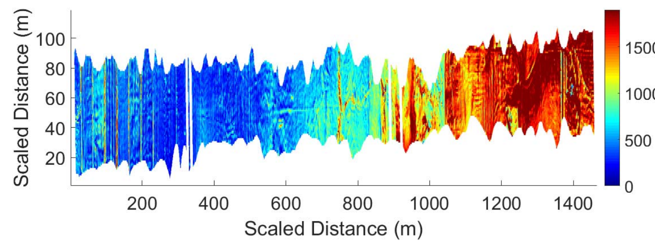

Fig. 5. Total AD across all 80 bands at each pixel in the overlap region between swaths 1 and 2 shown in Fig. 4. The mean offset per pixel per band is ~960 microflicks, which is a large difference when standard pixel values are on the order of 5000–6000 microflicks. (Right) East side of the image has a larger AD due to clouds shading only part of swath 2.

Computer Corporation, Los Angeles, CA, USA). This software used the manufacture provided calibration data (640 samples by 80 bands) to calibrate the hyperspectral data to absolute radiance as measured at the sensor, as well as using a vector-tracing algorithm to geocorrect the hyperspectral data to an accuracy of 6–10 m on the ground, which was limited by the GPS/INS sensor accuracy, the landscape terrain and the digital elevation modelbeing used (if applicable). Owing to the data storage technique used in the camera system, it was also necessary to mosaic the separate sections of data stored during a single flight path to obtain a single swath.

B. Spatial Processing Step 3: Single Swath Geocorrection

Using a freely available U.S. Geological Survey (USGS) 0.3-m resolution orthoimage as master data, persistent landscape features such as road crossings, field intersections, rock cairns and even gully boundaries were found and used as ground control points to further improve the spatial accuracy. The advantage of this approach is that it can be done without the necessity of physically accessing the location, presuming that master data exists that possesses sufficient resolution. Each flight path yielded a swath approximately 4400×500 m^2, which is larger than the 485-m width of a single line capture due to roll of the aircraft, and larger than the 4350-m final width due to having a data cushion before and after the test area. For each swath, it was possible to find at least 30 ground control points that could be directly correlated between the hyperspectral data and the master orthoimage. The georeferencing was performed in AutoSync Workstation, which is a module of ERDAS Imagine 15 (Hexagon Geospatial), and resulted in an overall root-mean-square error value of 3–5 m depending on the swath, which is an improvement over the GPS/INS correction. Fig. 3 shows the result of georeferencing two separate swaths to the master orthoimage.

C. Spatial Processing Step 4: Swath-to-Swath Radiometric Correction

The primary radiometric calibration issue to be dealt with before swaths can be mosaicked is the effects of changing illumination conditions between flight passes. Lighting conditions may change between flight passes for many reasons, such as high-altitude clouds, movement of the sun and imperfect auto-calibration of the hyperspectral imaging camera's shutter speed (which might be necessary to avoid saturated pixels). Two adjacent geocorrected swaths (first, southernmost and second, flight passes) were mosaicked together with no radiometric calibration are shown in Fig. 4. It can be seen in these data that the northern portion is darker than the southern portion and that this difference is present throughout, though less pronounced on the west side. During this data-collection flight, the pilot reported observing high-altitude cirrus clouds [48] drifting over the study area, which leads to the supposed conclusion that these clouds were the cause of the illumination difference. This discrepancy could be reduced by the addition of an upward-facing illumination sensor, but such a sensor is still a point measurement and may therefore miss lighting artifacts near the edges.

Fig. 5 shows, for each overlapping pixel, the absolute difference (AD) between the two adjacent swaths as shown in Fig. 4. The AD is the absolute value of the radiance difference between the nth band in the North and South swath summed over all 80 bands, such that

$$\mathrm{AD} = \sum_{n=1}^{80} |\mathrm{North}\,(n) - \mathrm{South}\,(n)| \tag{1}$$

where north(n) and south(n) are the radiance values of the nth band in the northern and southern swaths, respectively.

As expected from the false-color image (Fig. 4), the pixels on the east side have a larger AD than those on the west due to the cloud cover shading the east side more than the west causing a greater radiance difference between the northern

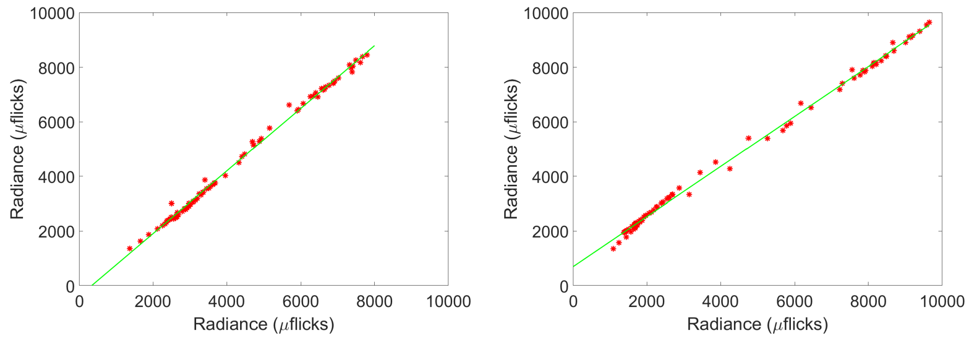

Fig. 6. Two examples of a single pixel of swath 1 plotted against the pixel from swath 2 at the same spatial location (red asterisks), and the corresponding linear fit (green lines) yielding the gain and bias necessary to correct pixel in swath 2 to match swath 1.

swath and the evenly illuminated southern swath. To remove slight misalignment issues owing to imperfect geocorrection and to save memory during processing, the overlap area was downsampled by a factor of 3 using the MATLAB "imresize" command utilizing the default bicubic interpolation method (see the Supplementary Online Material). This resizing reduced the memory requirements by a factor of 9 and improved processing time by at least the same factor.

On a pixel-by-pixel basis, the 80 hyperspectral bands of the southern swath (here chosen to be the master data), swath 1, are compared to the corresponding 80 bands of the northern swath, swath 2. Fitting a linear model to these data points yielded the gain and bias that corrects the radiance of the northern swath to that of the southern swath. Example pixels are shown in Fig. 6. This linear model was justified by the fact that the sensor is linear in intensity, regardless of wavelength, provided that it is not saturated. With these gain/bias values it was possible to modify each pixel in the northern swath to match the southern swath (to within the sensor noise) in the overlap area. It was then necessary to generalize the results to correct the entire northern swath.

To correct the northern swath, it was assumed that the illumination in an entire cross-track column (vertical line of pixels) was homogeneous and therefore could be corrected by the same gain and bias as those within the overlap region. Therefore, the gain and bias for each pixel in a cross-track column were averaged (vertical direction in Fig. 5) and are plotted in Fig. 7. These average gain and bias values were used to correct the radiance values of the northern swath to match the southern swath when applied to each cross-track column, where a perfectly matched illumination (and therefore radiance values) between adjacent regions would give a gain value of 1 and a bias of 0. Differences from these ideal values indicate differing illumination conditions between the regions. When observing a specific area under different illumination conditions, illumination variation will be seen as a difference in gain owing to the fact that the sensor is linear in intensity. Variation from an ideal bias is primarily owing to imperfectly matched pixels between the two swaths, which is most easily seen in Fig. 7 as the spikes on the west side of the image. These spikes are owing to a slight misalignment between the northern and southern swaths and can be attributed to pixels containing vegetation being compared to pixels containing bare ground and vice versa.

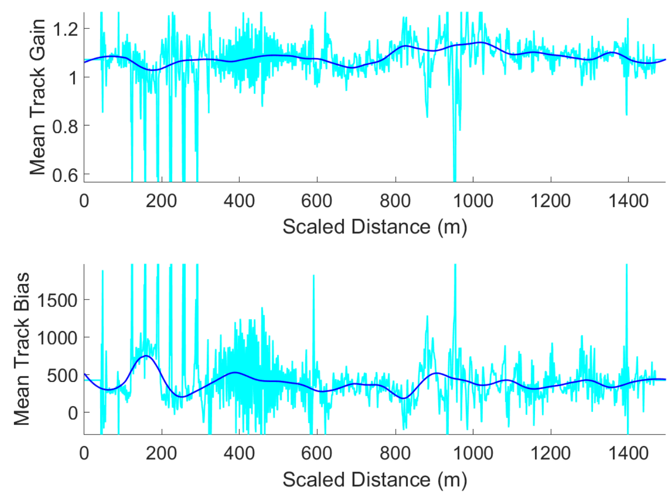

Fig. 7. (Top) Gain and (bottom) bias values are necessary to match the corresponding pixel in the northern swath to that of the southern swath averaged along the cross-track (vertical) direction. If the two swaths had identical illumination conditions, the gain would be exactly 1 and the bias would be 0, which is nearly the case in the regions where illumination was more similar between the swaths (left-hand side).

Similar issues can be seen at other field boundaries such as that around 600, where drastically different vegetation coverages are being compared between the two swaths. These artifacts can be reduced with improved geocorrection. Owing to these artifacts and using the assumption that illumination conditions vary smoothly over the area, a smoothing filter was employed. The "smooth" command in MATLAB was used with the "rloess" method, which is a local regression that uses weighted least squares and a second-degree polynomial that assigns zero weight to the data outside of six mean absolute deviations with a large 201 pixels-wide window. With the resizing factor, this 201 pixel-wide window was of roughly the same scale as the widths of the field in the sample area. Finally, the smoothed gain and bias were applied across the entire swath which corrected for the large-scale illumination disagreement existing between the two swaths along the flight direction.

To further correct the northern swath to match the southern swath, a cross-track adjustment was made assuming a simple linear model. This cross-track adjustment was made in the vertical direction and helped to remove slight vignette artifacts originating from the camera. While the cross-track adjustment was a minor change, it contributed to the overall agreement between the swaths. The adjustment had a slight

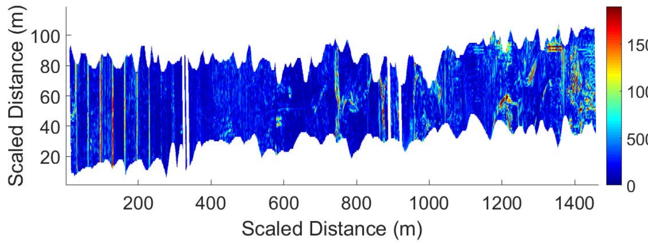

Fig. 8. Same overlap area in Fig. 7 after using the process to match the illumination (track and cross track) between the two swaths. The mean offset per pixel per band is ∼260 microflicks, which is a marked improvement over Fig. 7 and is similar to variance seen in uniform areas of the data.

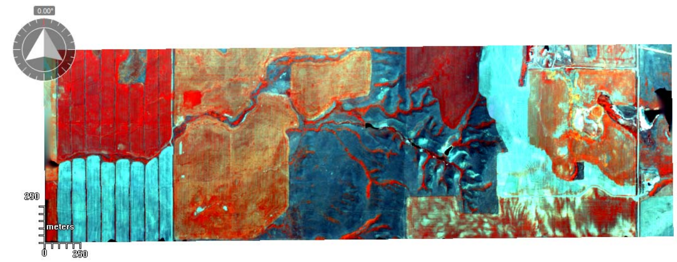

Fig. 9. Fully mosaicked data set consisting of four separate flight swaths taken over the course of 18 min. The radiance is self-consistent across the entire area but is lacking any absolute standard. The data is displayed with a standard deviation stretch in false-color IR using bands 10, 20, and 70 of the hyperspectral camera which correspond to 490.8, 554.7, and 874.2 nm.

tendency to change the overall illumination of the northern swath, however, and it was therefore necessary to complete a swath-wide illumination correction as a final step. These two corrections (here denoted as cross track and illumination) were implemented in MATLAB using the "fminsearch" command with a custom input function (see the Supplementary Online Material). This input function allowed for either a cross-track or illumination adjustment and returned a single figure of merit given by the total sum over all pixels of the AD between the northern and southern swath. By minimizing this figure of merit, the total agreement between the swaths on a pixel-by-pixel basis was maximized. The resulting parameters were applied to the entire northern swath, and the resulting corrected image is shown in Fig. 8, whose vertical scale is the same as that in Fig. 5. There are still regions of mismatched illumination in the image, mainly owing to bidirectional reflectance originating in areas with uneven terrain, such as gullies on the east side, and areas possessing a slight spatial mismatch, as shown in the fields on the west side. The average offset per pixel per band is reduced from 957 microflicks (before correction) to 265 microflicks (after correction), which is a factor of 3.6 improvement. The offset of 265 microflicks after correction is similar to the variation that exists within a single field and therefore may not be able to be significantly improved regardless of technique.

The overlap matching technique was fully automated and required no user input. This relative radiometric processing was continued across an entire test area to process as many swaths as may be required, which in this area was four swaths.

D. Spatial Processing Step 5: Large-Area Mosaicking

The individual swaths (now radiometrically calibrated to one another) were mosaicked in MosaicPro, which is a module of ERDAS Imagine 15. Seamlines in the image were generated based on the default values associated with the weighted seamline routine. If areas were missed owing to turbulence, the seamlines were adjusted manually to include these areas. To remove the gaps present in data collection, a routine in MATLAB was used to interpolate across the gaps on a band-by-band basis. A MATLAB routine based on directly solving a system of linear equations for ∇^2 across the gaps was used (see the Supplementary Online Material). After these processing steps, a complete data set of the entire test area was generated and is shown in Fig. 9. These data can now be analyzed as an entire unit of self-consistent radiometric data instead of four separate swaths possessing their own distinct radiometric ranges. These data are, however, lacking any absolute radiometric values, making it difficult to compare to other areas or to develop temporal trends in a quantitative manner.

E. Radiometric Processing Step 1: Transforming Hyperspectral Data From Radiance to Surface Reflectance

To convert the at-sensor radiance values, it is necessary to divide them by the solar irradiance as attenuated by the atmosphere to obtain surface reflectance data. A number of sophisticated models for this process exist, including MODerate resolution TRANsmission model [49], Atmospheric/Topographic CORrection [50], Atmospheric COrrection Now [51], Fast Line-of-sight Atmospheric AnalysiS of Hypercubes [52], and Simple Model of the Atmospheric Radiative Transfer of Sunshine [53], any of which could be used to calculate the atmospheric attenuation of the solar irradiance for calculation of surface reflectance. For simplicity, however, a model that was based on the ASTM G173-03 standard which contains reference solar spectral irradiance values [54] was chosen. This standard contains data for both the extraterrestrial (air mass 0) and terrestrial reference spectra at air mass 1.5 as calculated for a standard atmosphere and a rural aerosol profile, which fits the areas under investigation well. With these two sets of data and by assuming a linear relationship between them, it was possible at each wavelength to simulate on a very basic level any arbitrary air mass. It was then a simple matter to divide out the ground level solar irradiance from the hyperspectral data and to choose the appropriate air mass that minimizes the absorption features of O_2 observed in the hyperspectral data near 760 and 820 nm. The appropriate air mass is determined by minimizing the difference between the surface reflectance spectra and a smoothed version of the spectra effectively removing absorption features in the data (see the Supplementary Online Material).

Because such a large area was being examined, it was necessary to choose a subset of the data as a representative spectrum. Based on a simple normalized differential vegetation index (NDVI) [55]–[57] measurement, the top 15% most vegetative pixels (highest NDVI values) were chosen which, after averaging, gave a representative spectrum with very low noise that could then be used to determine the air mass necessary to best remove the O_2 absorption features. Given the strong absorption features present, it was also possible to calibrate

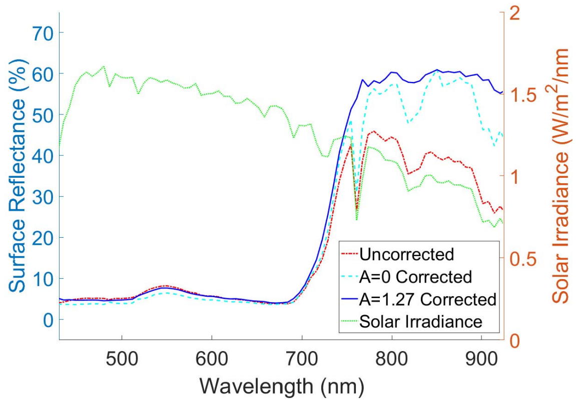

Fig. 10. Plot showing the uncorrected (scaled by mean value of extrasolar irradiance for display purposes) hyperspectral data (dotted dashed red curve), and the data corrected using the extraterrestrial solar irradiance ($A = 0$) (dashed cyan curve), the derived solar irradiance ($A = 1.27$) (solid blue curve), and the actual solar irradiance used for correction (dotted green curve). The derived solar irradiance removes absorption features quite effectively.

the wavelengths of the hyperspectral channels to provide more accurate data both in wavelength and surface reflectance. Once the air mass was determined, the entire area was scaled by dividing by the irradiance, which thereby yielded a surface reflectance data that could be directly compared to the LaSRC data. Results of this simple atmospheric model are shown in Fig. 10, which uses the average of the top 15% most vegetative pixels for both the extraterrestrial solar spectrum and the derived air mass spectrum. In the derivation, the result of an air mass value of 1.27 atmospheres due to a number of factors. One of these factors is that the sensor was not located at ground level, and therefore, the direct and scattered irradiance was different than the ASTM standard [54]. Another factor is that the elevation of the site was 1000 m above sea level and therefore possessed different O_2 columns than those of the standard.

F. Radiometric Processing Steps 2 and 3: Spatial Resampling of LaSRC Data and Hyperspectral Data

Using LaSRC as a radiometric reference target, it was possible to match the surface reflectance hyperspectral data to a trusted source despite the spatial, spectral, and reflectance differences between the two data sets. Initial processing was performed by ERDAS Imagine that used Rigorous Cubic Convolution to reproject the LaSRC data at 30-m resolution into the WGS 84/UTM zone 12N projection, which is the same projection as that of the hyperspectral data. These reprojected data were then used as a radiometric reference for the hyperspectral data. Ideally, hyperspectral flights would be coincident with Landsat data collection to remove the possibility that changes in the atmosphere would affect the data, but compromises must be made when coincident data collection is not possible. In this paper, the LaSRC data was acquired two days before the hyperspectral data on June 22, 2015.

To compare the hyperspectral data with its 1-m resolution to the 30-m resolution LaSRC data, both data sets were resampled via MATLAB to a common spatial resolution of 7.5 m using bicubic interpolation. This resampling to a spatial resolution of 7.5 m serves to create a common framework within which we can compare the two data sets at a spatial resolution wherein the LaSRC data can still be a trusted radiometric target and the reduced sampling of the hyperspectral is still a good representation of the data. The 1-m spatial resolution of the hyperspectral data was not abandoned but was temporarily reduced to allow a more direct comparison, as is discussed in Section III-J.

G. Radiometric Processing Step 4: Aligning LaSRC Data and Hyperspectral Data

One of the byproducts of interpolation is that the physical location of the terrain features can become distorted despite georeferencing both sets of data. Therefore, it was necessary to spatially shift one set of data to better match the other. This was accomplished via MATLAB using the built-in image transformation commands to estimate the geometric transformation between two 2-D grayscale images. The grayscale images were obtained directly from the red, green, and blue channels of the LaSRC data and from the equivalent three channels of the hyperspectral data after it was converted into the equivalent LaSRC bands (described in Section III-H). The grayscale hyperspectral image was registered to the grayscale LaSRC image in MATLAB using the "imregtform" command, which was constrained to only allow spatial translation. The resulting shifts were on the order of 10 m, which were less than the 30-m resolution of the LaSRC data and were therefore reasonable.

H. Radiometric Processing Step 5: Calculating LaSRC Equivalent Bands

The hyperspectral camera covers the spectral wavelength range 425–925 nm, within which six Landsat bands are contained. These Landsat bands include coastal blue, blue, green, red, IR, and the panchromatic band, of which the panchromatic band is not used in the processing as it is not included as part of the LaSRC data. The spectral response of these Landsat bands and a pair of adjacent hyperspectral bands are shown in Fig. 11. Each Landsat band covers multiple hyperspectral bands, with the coastal blue band covering six hyperspectral bands and the green band covering 16 hyperspectral bands, while some hyperspectral bands are outside the range of the Landsat bands. Using Landsat spectral response curves, it was possible to spectrally resample the hyperspectral data to directly correspond to the Landsat bands, which thereby allowed direct comparison between the hyperspectral and LaSRC data. A single Landsat equivalent channel ($\mathrm{LS}_{\mathrm{Equiv}}$) was obtained by multiplying the full spectral response curve ($\mathrm{LS}_{\mathrm{Resp}}$) by the hyperspectral values at each wavelength ($\mathrm{HS}(n)$) and by summing these values over all 80 bands. Lastly, the $\mathrm{LS}_{\mathrm{Equiv}}$ must be scaled by the ratio of the spectral width of the hyperspectral channels (fixed at 6.39 nm for this camera configuration) to the full width half max (FWHM) of the appropriate Landsat channel ($\mathrm{LS}_{\mathrm{FWHM}}$). This is represented by

$$\mathrm{LS}_{\mathrm{Equiv}} = \left(\sum_{n=1}^{80} \mathrm{LS}_{\mathrm{Resp}}(n) * \mathrm{HS}(n)\right) * 6.39/\mathrm{LS}_{\mathrm{FWHM}} \tag{2}$$

which gives the surface reflectance that a specific Landsat channel would see if it was observing the same spatial location observed by the hyperspectral camera.

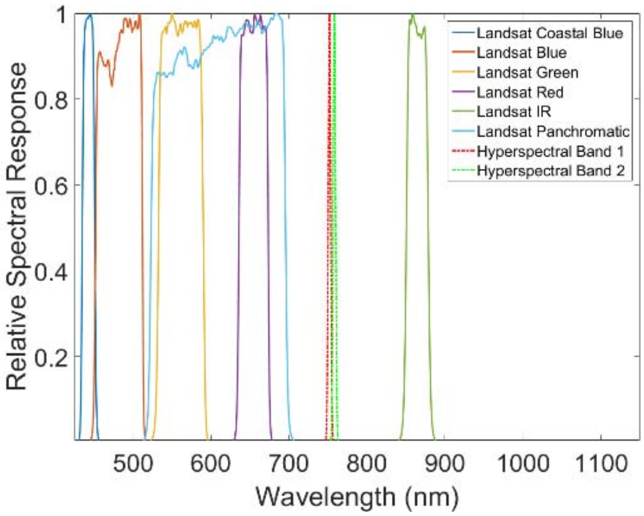

Fig. 11. Relative spectral response curves of the Landsat satellite (solid curves), and two adjacent bands from the hyperspectral camera (dashed curves).

I. Radiometric Processing Step 6: Determining the Gain/Bias to Best Match the Hyperspectral Data to LaSRC Data

The registered 7.5-m resolution LaSRC data was compared on a pixel-by-pixel basis to the corresponding 7.5-m resolution hyperspectral data pixel. An additional degree of freedom was provided wherein the hyperspectral data in each pixel could have a gain/bias applied in intensity space before being converted to its scaled Landsat equivalent

$$\mathrm{LS}_{\mathrm{Equiv,Scaled}} = \left[\sum_{n=1}^{80} \mathrm{LS}_{\mathrm{Resp}}(n) * (\mathrm{Gain} * \mathrm{HS}\,(n) + \mathrm{Bias})\right] * 6.39/\mathrm{LS}_{\mathrm{FWHM}}. \quad (3)$$

A linear model was used for the gain/bias because both sensors possessed a linear response in intensity, though they did not necessarily have the same responsivity or dark current. By changing the gain and bias for each pixel it was possible to minimize the difference between the scaled hyperspectral data and the LaSRC data, and to thereby radiometrically correct the hyperspectral data, using the LaSRC data as a reference, while preserving the information contained in the ratio of individual hyperspectral bands. To minimize the difference between the LaSRC data and the scaled hyperspectral data, the "fminsearch" command in MATLAB was used to search for the best gain and bias. For this it was necessary to write a custom MATLAB function (see the Supplementary Online Material) that took the hyperspectral data, the LaSRC data and the Landsat spectral response data as inputs and, after applying the gain and bias to the hyperspectral data, calculated the equivalent LaSRC response. This was identical to the processing described in Section III-H with the addition of applying the gain and bias to the hyperspectral data before calculating the LaSRC equivalent. The sum of the squared difference between the LaSRC data and the LaSRC equivalent data was weighted on a band-by-band basis based on the number of hyperspectral bands covered by a particular Landsat equivalent band. This weighting gave more weight to bands covering a larger wavelength range and less weight to bands such as Coastal Blue, which only overlaps with six hyperspectral bands. This number was minimized to determine the gain and bias that most precisely matched the hyperspectral data to the LaSRC data.

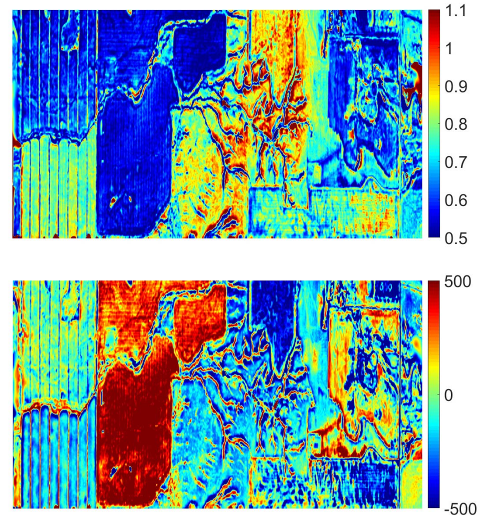

Fig. 12. Interpolated (top) gain and (bottom) bias determined by minimizing the difference between LaSRC data and the equivalent hyperspectral data. Values are smoothly varying across the image, so local contrast is maintained.

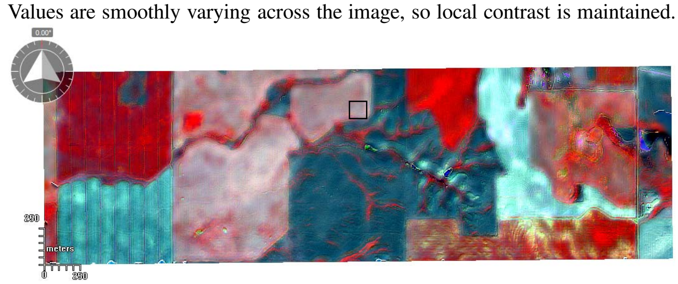

Fig. 13. Hyperspectral data after surface reflectance correction of five Landsat bands. Because the radiometric correction was performed with coarse resolution data, some of the small-scale saturation has been reduced and gives a more blurred appearance. The region in the black box is magnified in Fig. 17, showing the spatial resolution is maintained after processing. Mosaic is displayed with a standard deviation stretch as false-color IR using bands 10, 20, and 70 of the hyperspectral camera which correspond to 490.8, 554.7, and 874.2 nm.

J. Radiometric Processing Step 7: Correcting Hyperspectral Data From Interpolated Gain/Bias Values

Once the best gain and bias values were determined for each pixel (using the 7.5-m spatial resolution) the entire grid of gain and bias values was resized to the dimensions of the original data (i.e., back to 1-m spatial resolution) using "imresize" with bicubic interpolation. The interpolated gain and bias values for the entire area are shown in Fig. 12. The gain varies between approximately 0.5 and 1.1 for most of the image and is smoothly varying. The bias varies between −500 and 500 and with the scaling used (0%–100% covering a range of 0–10 000 as LaSRC data does) this range corresponds to ±5%. The interpolated values were then applied to each pixel of the hyperspectral data as a linear global spectral correction to create large-area radiometrically referenced surface reflectance hyperspectral data, as shown in Fig. 13.

IV. Results

To verify the spectral accuracy of this technique, ASD data was acquired for wheat at 17 separate locations around the Bozeman, MT, USA, test area and a representative spectrum was determined. This representative spectrum was used for comparison to 25 random pixels throughout the field. The test area was a uniformly managed wheat field and was expected to be uniform in terms of reflectance spectra and this was seen when examining the 25 random pixels. A comparison of two of these pixels (each 0.5 × 0.5 m) demonstrates the ASD data relative to the hyperspectral data before and after correction to LaSRC data as well as the actual LaSRC data at this same location is shown in Fig. 14, as well as the average error percent difference between the ASD data and the hyperspectral data for the 25 random pixels. The average percent difference over the 25 test areas was reduced from 4.16% before correction to 2.74% after correction to the LaSRC data. The agreement between the LaSRC data and the ASD data is good, especially considering the spatial resolution differences between the two sensors and the modeling necessary to get try surface reflectance data from the Landsat satellite. This measurement establishes an upper limit to the accuracy of the method, given the data available, as the LaSRC data was taken two days after the ASD data.

To spatially verify the accuracy of the hyperspectral data corrections, a range of sizes from 1–1681 m^2 (1- to 41-m squares on each edge) were tested. For each size 2000 areas were chosen at random and compared. In order to compare the range of sizes, the LaSRC data was resampled to a 1-m resolution using bicubic interpolation, though nearest neighbor was also tried and yielded similar results. The hyperspectral data was aligned to the 1-m spatial resolution LaSRC data as described in Section III-G. Areas were chosen at random from across the image and the mean values of the hyperspectral data within each square were computed. The mean hyperspectral data (after being transformed into the LaSRC equivalent) was then compared individually to the five LaSRC bands, and from these values, a mean absolute percentage error (MAPE) value was obtained for the various area sizes (see the Supplementary Online Material), as shown in Fig. 15. Despite the various sizes of the random test areas, the agreement of their MAPE value was consistent at all scales even though 30-m resolution data were used to correct 1-m resolution data. This comparison within the corrected data shows the significant agreement between the hyperspectral data and the LaSRC data in a quantitative sense.

When comparing data collected in two different and subsequent years, the value of using LaSRC data as a reference target becomes apparent. To compare the surface reflectance corrections, a large area of uniform vegetation coverage, from site C, was chosen and averaged over the spatial extent, and these data are plotted in Fig. 16 before and after correction for each of the two years. Looking at the LaSRC data (asterisks) in either graph, an increase can be seen in the reflectance throughout the visible wavelengths (400–700 nm) and a slight decrease can be seen in the NIR wavelengths (700–1000 nm). This conclusion could not be made with the hyperspectral data before the correction was made because the uncorrected plots from the two different years lie nearly on top of each other. After the surface reflectance corrections are applied to the data, however, the change in reflectance from 2014 to 2015 can easily be seen in the hyperspectral data. This simple example shows the value of using LaSRC as a radiometric reference target for hyperspectral data when undertaking a time-series analysis.

V. Discussion

Through a series of spatial and radiometric processing steps, large-area radiometrically corrected surface reflectance hyperspectral data are created. Nearly all the processing steps can be completed without user input, excepting geometric ground control point identification, demonstrating the potential of this process for automated monitoring of large areas. During processing, the first major obstacle was directly related to the inferiority of the GPS/INS precision compared to that of the pixel resolution. This required user input to geocorrect the hyperspectral data to a master orthoimage, as described in spatial processing 3 (Section III-B) with the end product shown in Fig. 3. Future improvements in this area could be made by using improved GPS/INS devices, gimbal-stabilized camera mounts, and machine vision developments to automate the alignment.

The second problem of note was the effects from nonuniform illumination conditions throughout the duration of multiple flight passes, which was compounded using autoexposure on the hyperspectral camera. This was addressed by creating a relatively simple model for the illumination condition changes between subsequent swaths, as described in spatial processing 4 (Section III-C). This model was derived purely from the hyperspectral data and did not require any additional information about cloud cover or autoexposure, which made it very robust and widely applicable. It does suffer from the assumption that there exists one swath that was evenly illuminated during the entire pass, but the effects of this assumption were accounted for by the subsequent surface reflectance correction.

The conversion of sensor radiance into surface reflectance is not a simple problem because the atmosphere is a very complex and constantly changing system. Significant strides are being made toward true surface level data even in the form of the LaSRC data product and, while the approximations used to correct this hyperspectral data to the surface reflectance used in this paper (Section III-E) are basic, more complex atmospheric modeling could easily be integrated into the processing pipeline.

Achieving the radiometric correction quality necessary to compare areas that are separated in space and/or time is not a trivial task, especially given the discrepancy between the spatial and spectral resolutions of the hyperspectral data and the high-quality satellite data. Spatial resampling is not a new idea and major ideas in this paper were borrowed from digital photography. More advanced resampling techniques such as edge sampling [58], new edge-directed interpolation [59], error-amended sharp edge [60], soft-decision adaptive interpolation [61], and Gaussian radial basis function [62] could improve the spatial quality of the final data. The best technique may be landscape dependent, however, and care should be taken in choosing resampling algorithms. Even with the relatively simple bicubic resampling used here (Section III-G), the agreement between the LaSRC data and the calibrated

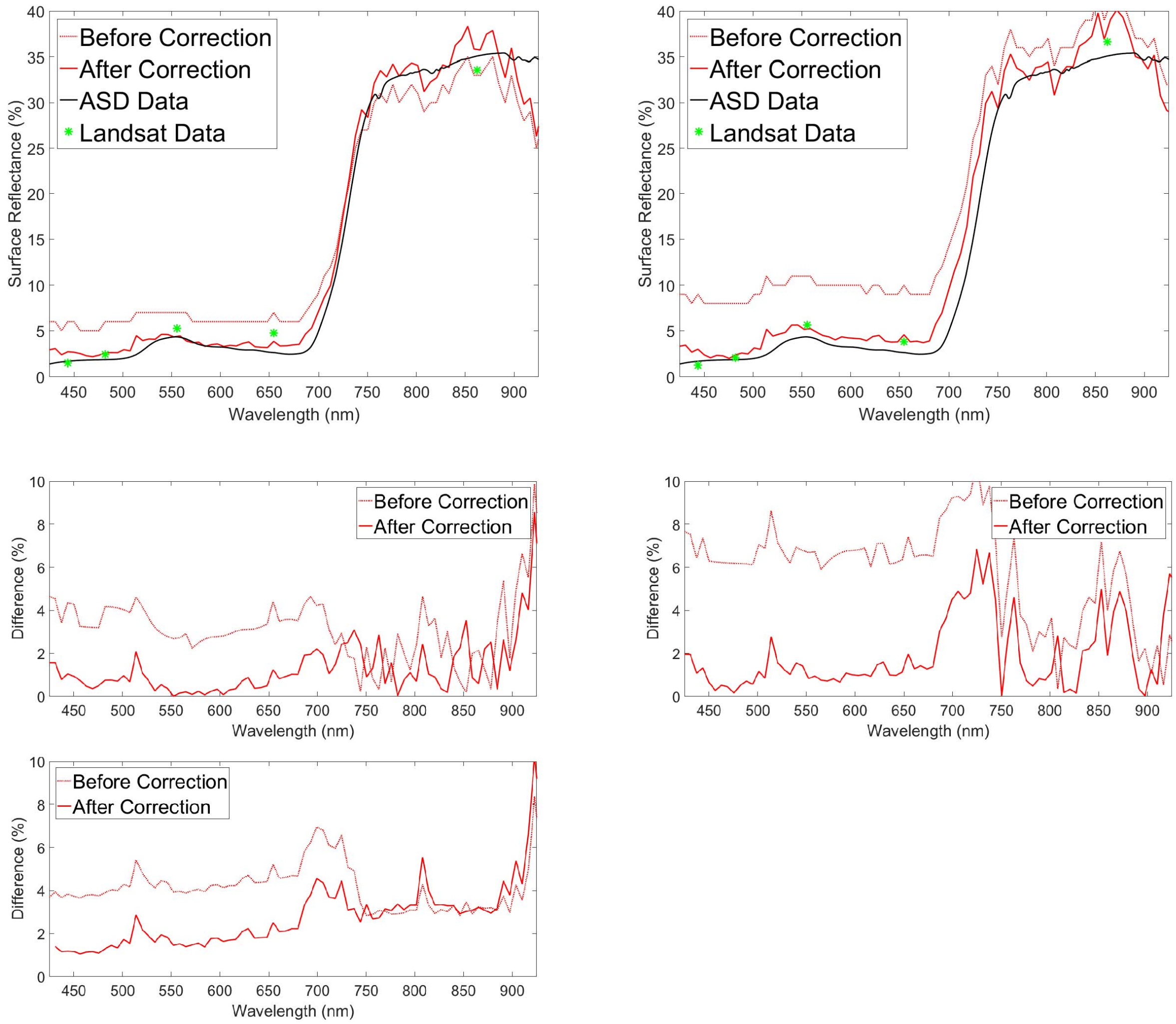

Fig. 14. (Top) Spectra of single pixels of a wheat field before (dotted red curve) and after (solid red curve) correction to LaSRC data compared to ASD data (black curve) and LaSRC data (green asterisks) for the same locations. Before correction data had the simple atmospheric model applied in order to more directly compare surface reflectance values. (Middle) Difference between hyperspectral data and ASD data before and after correction corresponding to the top graphs. (Bottom) Average difference between hyperspectral data and ASD data before and after correction.

hyperspectral data improved substantially, even down to the 1-m resolution scale, as shown in Fig. 15. The spectral resampling presented here is quite basic and could improve upon by more sophisticated models [63]. While the data appear to have a degraded spatial resolution (Fig. 13) upon closer examination (Fig. 17), it becomes obvious that the spatial resolution is unchanged and in some areas details emerge which were not readily visible before correction. However, in other areas, such as the fields in the left center of Fig. 13, the local contrast is reduced, leading to the overall appearance of blurring or loss of spatial resolution.

One of the potentially useful results in terms of absolute radiometric correction is illustrated in Fig. 16, which shows the difference between the calibrated and uncalibrated data taken one year apart. The hyperspectral data derive its radiometric values from the autoexposure algorithm of the camera (controlled by the shutter speed) and associated preflight laboratory calibrations that do not take into account changes in the sensor, lens, illumination conditions, or atmosphere. Neglect of these instrumentation and lighting changes can potentially cause the year-to-year vegetation reflectance changes to either be

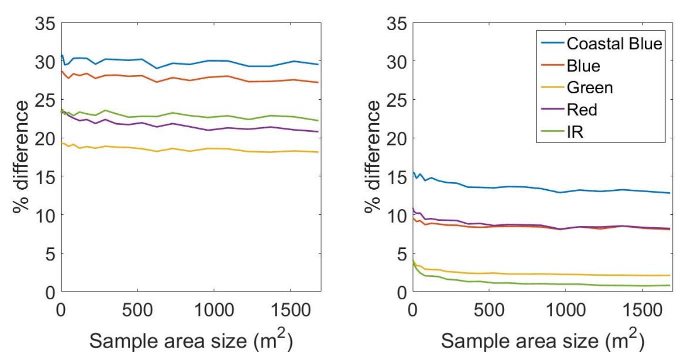

Fig. 15. MAPE between (Left) uncorrected and (Right) corrected hyperspectral data compared to LaSRC data averaged over 2000 random areas of varying sizes.

lost or exaggerated. With the addition of the LaSRC data and the processing techniques presented, a more complete story can be seen from year-to-year. This idea of radiometric calibration, especially to surface reflectance, is of great importance when trying to draw conclusions based upon temporal data.

While in this work LaSRC data were used as the surface reflectance reference (primarily due to the free access to high-

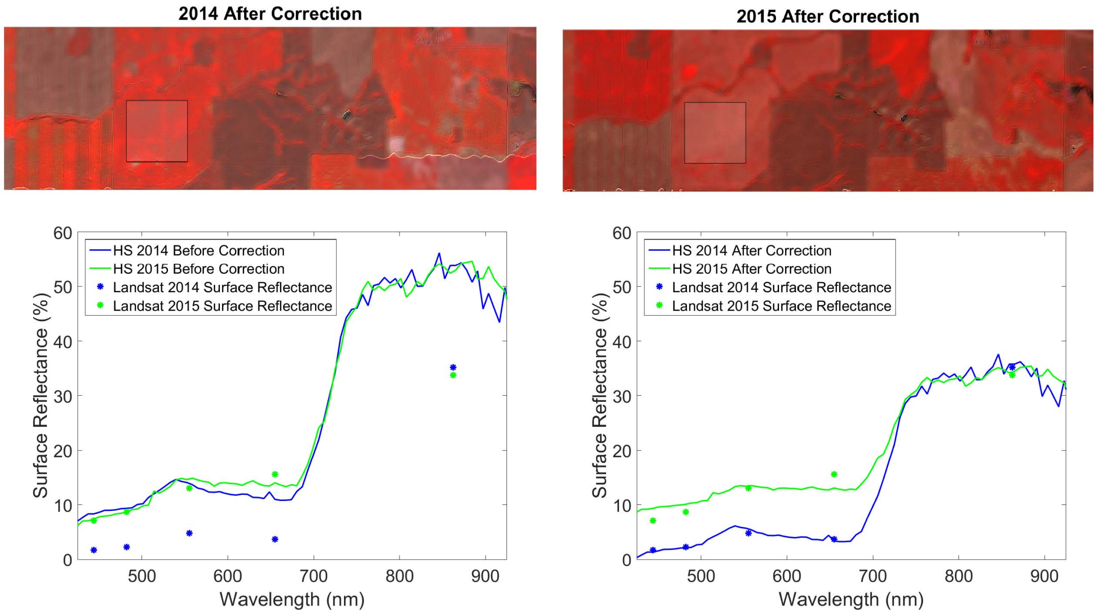

Fig. 16. (Top) False-color IR images of site C are displayed with the same manual dynamic range adjustment for each image using the average of bands 5–15, 15–25, and 65–75 of the hyperspectral data acquired from the same location in two different years (2014 and 2015) after geocorrection and radiometric correction. (Bottom) Hyperspectral data of a sample area (box in top images) plotted before and after correction to the LaSRC data showing the excellent agreement between the data. The sample area was chosen because the land area was uniform in coverage and vegetation type for both years. In the left graph, it is not possible using the hyperspectral data alone to come to any conclusion about changes in the data despite the fact that the LaSRC data would suggest changes were present. In the right graph, however, the change in the spectra can easily be seen in the hyperspectral data and agrees with the LaSRC data.

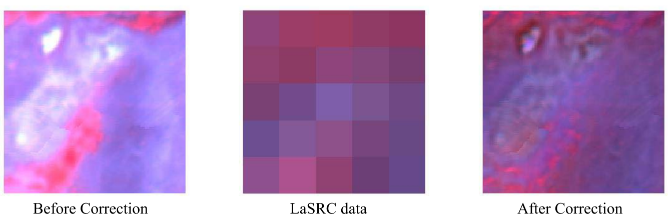

Fig. 17. All three images used the same manual dynamic range adjustment to display false-color IR images displayed using the average of bands 5–15, 15–25, and 65–75 of the hyperspectral camera before correction to (Left) LaSRC, and (Right) after correction and the false-color IR image using bands 5, 3, and 2 of the (Middle) LaSRC data. The region encompasses 25 Landsat pixels (5×5 grid measuring 150 m $\times$ 150 m) and the corresponding 22 500 hyperspectral pixels. The spatial resolution of the hyperspectral data is not degraded; though, the local contrast is reduced in some areas due to the spatial resampling. Image location is shown in Fig. 13 for reference.

quality surface reflectance data), this method can be used with other surface reflectance reference data provided that the necessary spectral response curves are available, the atmospheric correction from radiance to reflectance is sufficient for the problem, and the spatial resolution is adequate.

VI. Conclusion

Field calibration of hyperspectral imagery is difficult, and any method will have advantages and disadvantages. For example, placing a calibration target in the field such as a spectralon target with a well-defined reflectivity provides a reference spectrum that can be used to correct the flight-based hyperspectral imagery. These calibration targets provide excellent calibration near the target, but as one moves away from the target, the calibration becomes less certain. Thus a grid of targets is needed. Placing targets every 100 m (30 m) would require 1000 (11 000) targets to cover a 10 km^2 area. This number of targets becomes untenable for larger areas, particularly if site access is limited.

The bootstrap method described in this paper utilizes LaSRC surface reflectance data as a reference target for hyperspectral imagery. This technique relies on several reasonable assumptions. The first set of assumptions is aimed at rectifying the different spatial resolution of the LaSRC data product and the hyperspectral pixel resolution. The first of these two assumptions involves treating the hyperspectral imager as a linear imaging system. This assumption allows a reflectance spectrum to be generated by simply adding the reflectance spectra from several pixels together and dividing by the total number of pixels that are being combine. The second assumption is that the atmosphere changes little over the 30-m pixel resolution associated with the LaSRC surface reflectance data product. The second set of assumptions is aimed at rectifying the difference in the spectral resolution of the LaSRC data product and the hyperspectral imager. The LaSRC data product provides five spectral channels in the 425–925 nm spectral region (omitting the Landsat panchromatic band) while the hyperspectral imager provides 80 spectral channels. This implies that the LaSRC cannot be used to correct each spectral channel of the hyperspectral data independently. However, making the assumption that the responsivity of the hyperspectral imager and the Landsat imager are linear in intensity, the calibration can be completed as described in this paper. First, the hyperspectral data is combined to produce Landsat equivalent channels using a scaled responsivity, $\mathrm{R\_final} = G * \mathrm{R\_init} + \mathrm{B}$, where R_init is the initial reflectance, R_final is the final reflectance, G is the gain, and B is the bias, and the relative spectral responses of the Landsat channels. Then, G and B are adjusted to minimize the difference between the LaSRC data and the Landsat equivalent channels generated with the hyperspectral data for each pixel. This responsivity is then used to modify the entire hyperspectral spectral reflectance. Thus, the five spectral channels of the LaSRC data are used to generate the two parameters (overall gain and bias) needed to adjust the responsivity of the hyperspectral imager to provide the calibration correction. The advantages of this method include the 30-m grid of reference targets over large areas and minimizes the need for site access. The major disadvantage to this method is the fact that a linear correction is applied to the hyperspectral data which may miss higher order spectral corrections.

Field calibration of flight-based hyperspectral imagery is important for producing surface reflectance data over large areas. The most common method of field calibration involves the distribution of calibration targets such as spectralon to provide a well-defined reference surface reflectance for calibration. However, this method has disadvantages when trying to image large areas with limited site access. In this paper, a bootstrapping calibration technique was presented that can allow for calibration of large-area hyperspectral imagery. This method is based on three reasonable assumptions described above. Combining calibration methods such as distribution of calibration targets with the bootstrap method presented in this paper may provide a more robust calibration technique where limited site access and/or limited calibration targets are available.

The bootstrap method of calibration presented in this paper has been applied to several hyperspectral data sets at various field sites. At an agricultural field site, the calibration technique presented in this paper was compared to ASD data at seventeen locations. As seen in Fig. 14, correcting the hyperspectral data with an atmospheric model results in a 4.16% difference on average as comparted to the ASD data. After applying the calibration correction based on the method presented in this paper difference was reduced to 2.74% on average. This experimental validation lends credence to the calibration based on the linear responsivity correction based on comparing the Landsat equivalent channels with the LaSRC channels.

The ability to produce hyperspectral imagery over large areas using LaSRC data products as a surface reflectance reference was shown over a test area 5.78 km^2 in extent, but was also done at two nearby areas of 5.86 and 6.79 km^2 in extent giving a total area of approximately 18.4 km^2 that was calibrated. Furthermore, the hyperspectral data collected at this study site allows a temporal comparison of flight-based hyperspectral data.

Acknowledgment

Neither the U.S. Government nor any agency thereof, nor any of their employees, makes any warranty, express or implied, or assumes any legal liability or responsibility for the accuracy, completeness, or usefulness of any information, apparatus, product, or process disclosed, or represents that its use would not infringe privately owned rights. Reference herein to any specific commercial product, process, or service by trade name, trademark, manufacturer, or otherwise does not necessarily constitute or imply its endorsement, recommendation, or favoring by the United States Government or any agency thereof. The views and opinions of authors expressed herein do not necessarily state or reflect those of the U.S. Government or any agency thereof. Landsat data available from the USGS. LaSRC products courtesy of the USGS. The authors would like to thank the reviewers who have pushed this paper to be significantly better in terms of writing, information content, and impact. The authors thank them for their time and effort in this regard.

References

[1] G. A. Carter and A. K. Knapp, "Leaf optical properties in higher plants: Linking spectral characteristics to stress and chlorophyll concentration," *Amer. J. Botany*, vol. 88, no. 4, pp. 677–684, 2001.

[2] W. K. Smith, T. C. Vogelmann, E. H. DeLucia, D. T. Bell, and K. A. Shepherd, "Leaf form and photosynthesis," *BioScience*, vol. 47, no. 11, pp. 785–793, 1997.

[3] P. Zarco-Tejada, "Chlorophyll fluorescence effects on vegetation apparent reflectance: I. Leaf-level measurements and model simulation," *Remote Sens. Environ.*, vol. 74, no. 3, pp. 582–595, 2000.

[4] J. Peñuelas, I. Filella, C. Biel, R. Savé, and L. Serrano, "The reflectance at the 950–970 nm region as an indicator of plant water status," *Int. J. Remote Sens.*, vol. 14, no. 10, pp. 1887–1905, 1993.

[5] L. S. Galvão, M. A. Pizarro, and J. C. N. Epiphanio, "Variations in reflectance of tropical soils: Spectral-chemical composition relationships from AVIRIS data," *Remote Sens. Environ.*, vol. 75, no. 2, pp. 245–255, 2001.

[6] D. Summers, M. Lewis, B. Ostendorf, and D. Chittleborough, "Visible near-infrared reflectance spectroscopy as a predictive indicator of soil properties," *Ecol. Indicators*, vol. 11, no. 1, pp. 123–131, 2011.

[7] I. Strachan, E. Pattey, and J. B. Boisvert, "Impact of nitrogen and environmental conditions on corn as detected by hyperspectral reflectance," *Remote Sens. Environ.*, vol. 80, no. 2, pp. 213–224, 2002.

[8] D. Haboudane, J. R. Miller, E. Pattey, P. J. Zarco-Tejada, and I. B. Strachan, "Hyperspectral vegetation indices and novel algorithms for predicting green LAI of crop canopies: Modeling and validation in the context of precision agriculture," *Remote Sens. Environ.*, vol. 90, no. 3, pp. 337–352, 2004.

[9] N. Gat *et al.*, "Estimating sugar beet yield using AVIRIS-derived indices," in *Proc. 9th JPL Airborne Earth Sci. Workshop*, Pasadena, CA, USA, 2000.

[10] C. Yang, "Airborne hyperspectral imagery for mapping crop yield variability," *Geography Compass*, vol. 3, no. 5, pp. 1717–1731, 2009.

[11] A. Bannari, A. Pacheco, K. Staenz, H. McNairn, and K. Omari, "Estimating and mapping crop residues cover on agricultural lands using hyperspectral and IKONOS data," *Remote Sens. Environ.*, vol. 104, no. 4, pp. 447–459, 2006.

[12] P. Evangelista, T. J. Stohlgren, J. T. Morisette, and S. Kumar, "Mapping invasive tamarisk (tamarix): A comparison of single-scene and time-series analyses of remotely sensed data," *Remote Sens.*, vol. 1, no. 3, pp. 519–533, 2009.

[13] L. Wang, "Invasive species spread mapping using multi-resolution remote sensing data," in *Proc. Int. Arch. Photogram., Remote Sens. Spatial Inf. Sci.*, vol. 37. Beijing, China, 2008, pp. 135–142.

[14] R. Lawrence and M. Labus, "Early detection of Douglas-fir beetle infestation with subcanopy resolution hyperspectral imagery," *Western J. Appl. Forestry*, vol. 18, no. 3, pp. 202–206, 2003.

[15] P. H. Sampson, P. J. Zarco-Tejada, G. H. Mohammed, J. R. Miller, and T. L. Noland, "Hyperspectral remote sensing of forest condition: Estimating chlorophyll content in tolerant hardwoods," *Forest Sci.*, vol. 49, no. 3, pp. 381–391, 2003.

[16] G. A. Carter and R. L. Miller, "Early detection of plant stress by digital imaging within narrow stress-sensitive wavebands," *Remote Sens. Environ.*, vol. 50, no. 3, pp. 295–302, 1994.

[17] K. L. Smith, M. D. Steven, and J. J. Colls, "Use of hyperspectral derivative ratios in the red-edge region to identify plant stress responses to gas leaks," *Remote Sens. Environ.*, vol. 92, no. 2, pp. 207–217, 2004.

[18] C. J. Keith, K. S. Repasky, R. L. Lawrence, S. C. Jay, and J. L. Carlsten, "Monitoring effects of a controlled subsurface carbon dioxide release on vegetation using a hyperspectral imager," *Int. J. Greenhouse Gas Control*, vol. 3, no. 5, pp. 626–632, 2009.

[19] M. F. Noomen, K. L. Smith, J. J. Colls, M. D. Steven, A. K. Skidmore, and F. D. van der Meer, "Hyperspectral indices for detecting changes in canopy reflectance as a result of underground natural gas leakage," *Int. J. Remote Sens.*, vol. 29, no. 20, pp. 5987–6008, 2008.

[20] J. Rouse *et al.*, "Multi-spectral imaging of vegetation for detecting CO_2 leaking from underground," *Environ. Earth Sci.*, vol. 60, no. 2, pp. 313–323, 2010.

[21] L. Bateson *et al.*, "The application of remote-sensing techniques to monitor CO_2-storage sites for surface leakage: Method development and testing at Latera (Italy) where naturally produced CO_2 is leaking to the atmosphere," *Int. J. Greenhouse Gas Control*, vol. 2, no. 3, pp. 388–400, 2008.

[22] E. Male *et al.*, "Using hyperspectral plant signatures for CO_2 leak detection during the 2008 ZERT CO_2 sequestration field experiment in Bozeman, Montana," *Environ. Earth Sci.*, vol. 60, no. 2, pp. 251–261, 2010.

[23] G. J. Bellante, S. L. Powell, R. L. Lawrence, K. S. Repasky, and T. A. Dougher, "Aerial detection of a simulated CO_2 leak from a geologic sequestration site using hyperspectral imagery," *Int. J. Greenhouse Gas Control*, vol. 13, pp. 124–137, Mar. 2013.

[24] G. Bellante *et al.*, "Hyperspectral detection of a subsurface CO_2 leak in the presence of water stressed vegetation," *PLoS ONE*, vol. 9, no. 10, p. e108299, 2014.

[25] X. Z. Shi, M. Aspandiar, and D. Oldmeadow, "Using hyperspectral data and PLSR modelling to assess acid sulphate soil in subsurface," *J. Soils Sediments*, vol. 14, no. 5, pp. 904–916, 2014.

[26] F. A. Kruse, A. B. Lefkoff, and J. B. Dietz, "Expert system-based mineral mapping in northern death valley, California/Nevada, using the airborne visible/infrared imaging spectrometer (AVIRIS)," *Remote Sens. Environ.*, vol. 44, nos. 2–3, pp. 309–336, Jun. 1993.

[27] R. Richter, "Hyperspectral sensors for military applications," German Aerospace Center Wessling (DLR), Wessling, Germany, Tech. Rep. ADA469649, 2005.

[28] R. Hruska, J. Mitchell, M. Anderson, and N. F. Glenn, "Radiometric and geometric analysis of hyperspectral imagery acquired from an unmanned aerial vehicle," *Remote Sens.*, vol. 4, no. 9, pp. 2736–2752, 2012.

[29] E. Knight and G. Kvaran, "Landsat-8 operational land imager design, characterization and performance," *Remote Sens.*, vol. 6, no. 11, pp. 10286–10305, 2014.

[30] D. P. Roy *et al.*, "Landsat-8: Science and product vision for terrestrial global change research," *Remote Sens. Environ.*, vol. 145, pp. 154–172, Apr. 2014.

[31] M. A. Folkman *et al.*, "EO-1/Hyperion hyperspectral imager design, development, characterization, and calibration," *Proc. SPIE*, vol. 4151, pp. 40–51, Feb. 2001.

[32] J. S. Pearlman, P. S. Barry, C. C. Segal, J. Shepanski, D. Beiso, and S. L. Carman, "Hyperion, a space-based imaging spectrometer," *IEEE Trans. Geosci. Remote Sens.*, vol. 41, no. 6, pp. 1160–1173, Jun. 2003.

[33] (2016). *AVIRIS—Airborne Visible/Infrared Imaging Spectrometer—General Overview*, accessed on Jan. 17, 2016. [Online]. Available: http://aviris.jpl.nasa.gov/aviris/

[34] D. Olsen, C. Dou, X. Zhang, L. Hu, H. Kim, and E. Hildum, "Radiometric calibration for AgCam," *Remote Sens.*, vol. 2, no. 2, pp. 464–477, 2010.

[35] M. Dinguirard and P. N. Slater, "Calibration of space-multispectral imaging sensors: A review," *Remote Sens. Environ.*, vol. 68, no. 3, pp. 194–205, 1999.

[36] T. Cocks, R. Jenssen, A. Stewart, I. Wilson, and T. Shields, "The HyMap airborne hyperspectral sensor: The system, calibration and performance," in *Proc. 1st EARSEL Workshop Imag. Spectroscopy*, Zürich, Switzerland, 1998, pp. 37–42.

[37] A. Asmat, E. J. Milton, and P. M. Atkinson, "Empirical correction of multiple flightline hyperspectral aerial image mosaics," *Remote Sens. Environ.*, vol. 115, no. 10, pp. 2664–2673, 2011.

[38] L. Markelin, E. Honkavaara, T. Takala, and P. Pellikka, "Calibration and validation of hyperspectral imagery using permanent test field," in *Proc. 5th Workshop Hyperspectral Image Signal Process., Evol. Remote Sens. (WHISPERS)*, Gainesville, FL, USA, 2013, pp. 1–4.

[39] H. Li, H. Zhang, B. Zhang, Z. Chen, M. Yang, and Y. Zhang, "A method suitable for vicarious calibration of a UAV hyperspectral remote sensor," *IEEE J. Sel. Topics Appl. Earth Observ. Remote Sens.*, vol. 8, no. 6, pp. 3209–3223, Jun. 2015.

[40] I. Mednieks, "A method for correction of rural multispectral aerial image mosaics," in *Proc. 13th Biennial Baltic Electron. Conf. (BEC)*, Oct. 2012, pp. 295–298.

[41] C. M. Gevaert, J. Suomalainen, J. Tang, and L. Kooistra, "Generation of spectral–temporal response surfaces by combining multispectral satellite and hyperspectral UAV imagery for precision agriculture applications," *IEEE J. Sel. Topics Appl. Earth Observ. Remote Sens.*, vol. 8, no. 6, pp. 3140–3146, Jun. 2015.

[42] J. Barsi, K. Lee, G. Kvaran, B. L. Markham, and J. A. Pedelty, "The spectral response of the landsat-8 operational land imager," *Remote Sens.*, vol. 6, no. 10, pp. 10232–10251, 2014.

[43] B. Markham *et al.*, "Landsat-8 operational land imager radiometric calibration and stability," *Remote Sens.*, vol. 6, no. 12, pp. 12275–12308, 2014.

[44] J. C. Storey, M. J. Choate, and K. Lee, "Landsat 8 operational land imager on-orbit geometric calibration and performance," *Remote Sens.*, vol. 6, no. 11, pp. 11127–11152, 2014.

[45] P. Thenkabail, *Hyperspectral Remote Sensing of Vegetation*. Boca Raton, FL, USA: CRC Press, 2012.

[46] J. Gao, *Digital Analysis of Remotely Sensed Imagery*. New York, NY, USA: McGraw-Hill, 2009.

[47] M. Eismann, *Hyperspectral Remote Sensing*. Bellingham WA, USA: SPIE, 2012.

[48] M. A. Vaughan, Z. Liu, M. J. McGill, Y. Hu, and M. D. Obland, "On the spectral dependence of backscatter from cirrus clouds: Assessing CALIOP's 1064 nm calibration assumptions using cloud physics lidar measurements," *J. Geophys. Res., Atmos.*, vol. 115, no. D14, pp. 2156–2202, 2010.

[49] A. Berk *et al.*, "MODTRAN 5: A reformulated atmospheric band model with auxiliary species and practical multiple scattering options: Update," *Proc. SPIE*, vol. 5806, pp. 662–667, Jul. 2005.

[50] R. Richter and D. Schlapfer, "Atmospheric/topographic correction for airborne imagery: ATCOR-4 user guide," DLR IB, Tech. Rep. 565-02, 2012.

[51] R. Green, "Atmospheric correction now (ACORN)," developed by ImSpec LLC, available from Analytical Imaging and Geophysics LLC, Boulder, CO, USA, 2001.

[52] T. Cooley *et al.*, "FLAASH, a MODTRAN4-based atmospheric correction algorithm, its application and validation," in *Proc. IEEE Int. Geosci. Remote Sens. Symp. (IGARSS)*, vol. 3. Jun. 2002, pp. 1414–1418.

[53] C. A. Gueymard. (2005). *SMARTS Code, Version 2.9.5 User's Manual*. [Online]. Available: http://www.solarconsultingservices.com/SMARTS295_manual.pdf

[54] G173-03 (Reapproved 2012), *Standard Tables for Reference Solar Spectral Irradiances: Direct Normal and Hemispherical on 37° Tilted Surface*, ASTM Standard G173-03, 2012.

[55] T. N. Carlson and D. A. Ripley, "On the relation between NDVI, fractional vegetation cover, and leaf area index," *Remote Sens. Environ.*, vol. 62, no. 3, pp. 241–252, 1997.

[56] R. S. DeFries and J. R. G. Townshend, "NDVI-derived land cover classifications at a global scale," *Int. J. Remote Sens.*, vol. 15, no. 17, pp. 3567–3586, 1994.

[57] M. Wójtowicz, A. Wójtowicz, and J. Piekarczyk, "Application of remote sensing methods in agriculture," *Commun. Biometry Crop Sci.*, vol. 11, no. 1, pp. 31–50, 2016.

[58] R. Fattal, "Image upsampling via imposed edge statistics," *ACM Trans. Graph.*, vol. 26, no. 3, 2007, Art. no. 95.

[59] X. Li and M. T. Orchard, "New edge-directed interpolation," *IEEE Trans. Image Process.*, vol. 10, no. 10, pp. 1521–1527, Oct. 2001.

[60] Y. Cha and S. Kim, "The error-amended sharp edge (EASE) scheme for image zooming," *IEEE Trans. Image Process.*, vol. 16, no. 6, pp. 1496–1505, Jun. 2007.

[61] X. Zhang and X. Wu, "Image interpolation by adaptive 2-D autoregressive modeling and soft-decision estimation," *IEEE Trans. Image Process.*, vol. 17, no. 6, pp. 887–896, Jun. 2008.

[62] Y. J. Lee and J. Yoon, "Nonlinear image upsampling method based on radial basis function interpolation," *IEEE Trans. Image Process.*, vol. 19, no. 10, pp. 2682–2692, Oct. 2010.

[63] H. Zhao, G. Jia, and N. Li, "Transformation from hyperspectral radiance data to data of other sensors based on spectral superresolution," *IEEE Trans. Geosci. Remote Sens.*, vol. 48, no. 11, pp. 3903–3912, Nov. 2010.

Cooper McCann, photograph and biography not available at the time of publication.

Kevin S. Repasky, photograph and biography not available at the time of publication.

Mikindra Morin, photograph and biography not available at the time of publication.

Rick L. Lawrence, photograph and biography not available at the time of publication.

Scott Powell, photograph and biography not available at the time of publication.